HAL
open science

Evidence for a build-in remnant field in symmetrically contacted MAPbB_3 X-ray detectors

Ferdinand Ledee, Javier-Alejandro Mayen Guillen, Stephanie Lombard, Julien Zaccaro, Jean-Marie Verilhac, Eric Gros d'Aillon

To cite this version:

Ferdinand Ledee, Javier-Alejandro Mayen Guillen, Stephanie Lombard, Julien Zaccaro, Jean-Marie Verilhac, et al.. Evidence for a build-in remnant field in symmetrically contacted MAPbB_3 X-ray detectors. Journal of Applied Physics, 2023, 134, pp.195703. 10.1063/5.0170580 . cea-04468082

HAL Id: cea-04468082

https://cea.hal.science/cea-04468082v1

Submitted on 20 Feb 2024

HAL is a multi-disciplinary open access archive for the deposit and dissemination of scientific research documents, whether they are published or not. The documents may come from teaching and research institutions in France or abroad, or from public or private research centers.

L'archive ouverte pluridisciplinaire **HAL**, est destinée au dépôt et à la diffusion de documents scientifiques de niveau recherche, publiés ou non, émanant des établissements d'enseignement et de recherche français ou étrangers, des laboratoires publics ou privés.

Evidence for a build-in remnant field in symmetrically contacted $MAPbBr_3$ X-ray detectors

Ferdinand Lédée[1,2,*], Javier Mayén-Guillen[2], Stéphanie Lombard[2], Julien Zacarro[3], Jean-Marie Verilhac[2], Eric Gros-Daillon[1,*]

[1] Grenoble Alpes University, CEA, LETI, DOPT, F38000 Grenoble, France

[2] Grenoble Alpes University, CEA, LITEN, DTNM, F38000 Grenoble, France

[3] Grenoble Alpes University, CNRS, Grenoble INP, Institut Néel, F38042 Grenoble, France

[*] ferdinand.ledee@cea.fr ; eric.grosdaillon@cea.fr

Keywords: X-ray detectors, halide perovskites, sensitivity, simulation, Hecht equation

1. Abstract

Millimeter-thick methylammonium lead tribromide ($MAPbBr_3$) single crystal X-ray detectors have recently raised attention due their high X-ray attenuation efficiency and good charge transport properties. However, an intriguing feature of the photocurrent response of $MAPbBr_3$ detectors has been largely overlooked in the literature. After biaising, transient sensitivity is measured under X-rays at short-circuit (Bias = 0V), thus revealing a large remnant electric field that build-up under bias. Here, we exploit the X-ray sensitivity of $MAPbBr_3$ detectors at zero-bias in order to probe the internal built-in field, as well as to investigate the charge transport properties of the perovskite material. Our model derived from the Hecht equation is able to fully rationalize the response of the detectors both at short-circuit and under moderate applied bias. Moreover, we provide a method for the estimation of the internal electric field, and for the sum of the electrons and holes mobility-lifetime products $\mu_e\tau_e + \mu_h\tau_h$. This general method could extend to any perovskite-based X-ray detector exhibiting transient sensitivity at zero-bias.

2. Introduction

Metal halide perovskites are the current key players in the field of radiation detection, challenging the performance of classical semiconductors in several applications while maintaining competitive manufacturing costs. In particular, methylammonium lead tribromide ($MAPbBr_3$) in single crystal form is one of the most intensively studied emerging material for the direct detection of X-rays.[1]–[7] Despite the high quality of these as-grown single crystals,[8]–[10] several features of this semiconducting material remain unexplained. Notably, in some cases the photocurrent response of $MAPbBr_3$ seems to deviate from the Hecht model.[1], [3], [4], [6] Hecht model is the most widely used model to describe the photoresponse of semiconductor-based X-rays detectors such as CdTe, CdZnTe,

GaAs; and shall be applied as well to halide perovskites.[11]–[13] In particular for $MAPbBr_3$, it is often applied in the form displayed in Eq. (2) to fit the experimental sensitivity-voltage (*S-V*) dataplots in order to extract the mobility-lifetime product $\mu\tau$ of the electronic charge carriers.[1], [2], [14], [15] Yet, previous work from our group revealed that the X-ray photoresponse of Cr/$MAPbBr_3$/Cr devices is not in accordance with the Hecht model.[16] Moreover, in the recent work of Alvarez *et al,* it is shown that sizeable X-ray photocurrent can be measured in Cr/$MAPbBr_3$/Cr devices in short-circuit conditions. Unlike photovoltaic-inspired devices that provide stable photocurrent output under irradiation,[17], [18] the X-ray photocurrent measured in Cr/$MAPbBr_3$/Cr photoconductors at zero-bias decays over time and follows the relaxation dynamics of the dark current.[19] We propose that this is the outcome of a residual electric field created upon biasing that relaxes when the bias is removed. This residual field would originate from the build-up of a space-charge when the Cr/$MAPbBr_3$/Cr device is biased, and would result in a diminished net applied electric field under operation. The internal electric field would be responsible for the anomalies listed above, in particular the discrepancy between the experimental sensitivity-voltage (S-V) data and the Eq. (2).

This paper aims to provide a detailed picture of the X-ray photoresponse of Cr/$MAPbBr_3$/Cr single crystal devices under short-circuit conditions. Starting from the assumption that the residual electric field prevalent at zero-bias is also present under an externally applied bias, we developed a model derived from the Hecht model that is able to assess with great precision the internal electric field that opposes the externally applied bias under operation. In addition, we use our model to bring an alternative pathway to establish relevant intervals for the $\mu\tau$ products in $MAPbBr_3$-based detectors. We believe that this work sheds new light on the X-ray photoresponse of $MAPbBr_3$ detectors; and will gives new insights into the residual charges that are formed in millimeter-thick lead halide perovskite devices under bias, as well as their aftermath on the detection performances.

3. Discussion on the internal electric field

In a semiconductor-based planar detector, the photocurrent measured under X-ray results from the induction of current by the photogenerated charges on the contact electrodes, also referred as the Ramo-Shockley theorem.[20] The integration of the photocurrent over the X-ray pulse duration brings one of the methods that allow to estimate the sensitivity, hereby expressed in µC mGy^{-1} cm^{-2}. Without any trapping, the sensitivity reaches a maximum value and depends only on the amount of photogenerated charges in the semiconductor :

$$S_0 = \int s_0(x)dx \tag{1}$$

With s_0 the charge generated in an elemental volume dx of the semiconductor (see Methods section). With trapping and for a planar detector with two facing electrodes, the analytical integration of the Ramo theorem over the charge carrier lifetime τ gives the sensitivity-voltage (*S-V*) relationship which reads:

$$S(V) = \frac{S_0\mu\tau V}{L^2}\left[1 - exp\left(-\frac{L^2}{\mu\tau V}\right)\right] \tag{2}$$

With S_0 the maximum sensitivity, μ the charge carrier mobility, V the applied bias and L the distance between the electrodes. This relation is only valid when the following conditions are met altogether i) the energy is absorbed close to the irradiated electrode ; ii) only one type of charge carrier drifts in the

device; iii) the electric field is uniform.[11] When the photocurrent contribution from the second charge carrier type cannot be neglected, e.g. when the absorption length is not negligible with respect to L, the relation becomes a function of the depth. It translates into the two-carriers Hecht equation which reads:

$$\eta(x,V) = \frac{\mu_e \tau_e V}{L^2}\left[1 - e^{-\frac{xL}{\mu_e \tau_e V}}\right] + \frac{\mu_h \tau_h V}{L^2}\left[1 - e^{-\frac{L(L-x)}{\mu_h \tau_h V}}\right] \quad (3)$$

Where η is the charge induction efficiency (CIE), x is the position of creation of the charge carriers (0<x<L), and the subscripts e and h denote for electrons and holes, respectively. The *S-V* relationship now reads :

$$S(V) = \int s_0(x)\eta(x,V)dx \quad (4)$$

With s_0 the charge generated in an elemental volume dx of the semiconductor (see Methods section). Further details on the fabrication of the detector, on the Hecht model and calculation of S_0 are provided in the Methods section.

A common approach in the research applied to perovskite X-ray detectors consists of using equation (2) or (4) to fit the experimental sensitivity-voltage data in order to extract a value for the mobility-lifetime product $\mu\tau$. In most of the works, the maximum sensitivity S_0 (or the maximum induced current I_0) is not estimated, and thus is set as a free parameter in the Hecht fits. We propose that this produces a lot of misinterpretation of the *S-V* data. As an illustration, Fig. 1 displays experimental *S-V* curve for a $MAPbBr_3$ single crystal planar detector fitted both with and without a calibrated and fixed S_0 value. The $\mu\tau$ product for electrons extracted from the fit differs by almost an order of magnitude depending on the method. Furthermore, in Figure 1b, the Hecht model is not in good accordance with the experimental *S-V*. The experimental sensitivity measured at higher biases is lower than the value predicted with the Hecht model, and seems to plateau to a much lower value than S_0 (typically $S_{max} = 0.25\ S_0$). Here the S_0 value has been estimated using Klein's rule (W = 14/5*Eg + 0.5)[21], however choosing a W value equal to that experimentally determined for $CsPbBr_3$ by He *et al.* does not change the result of the fit (see Fig. S1 for further details).[22] Furthermore, the Many equation also fails to fit our experimental S-V data (Fig. S4). This behavior has already been observed by our group for all our $MAPbBr_3$-based devices, as well as for various perovskite compositions.[16] The plateau of the sensitivity to a lower S value in $MAPbBr_3$-based devices is overlooked in the literature because the maximum sensitivity S_0 (or I_0) is mostly set as a free parameters as in Fig.1a.[1] Note that in that case, the S_0 value is not linked to any macroscopic quantity. Besides, *S-V* graphs are often plotted in semi-log scale, which misleads the reader into thinking that the fit is better than it actually is (see Fig.S2 for an illustration). [1], [2], [14] Remarkably, we carried out a *S-V* measurement adding a depolarization time (bias =0V) inbetween each bias step. Despite the relatively long (5-10 min) depolarization time and the relatively short (≈ 5s) bias pulse duration, the low S_{max} plateau is still present and the Hecht equation fails to fit the results (see Fig. S3 for further details). We attribute the plateau at lower S_0 value to a non-uniform electric field across the detector at higher applied bias. Several phenomena may distort the electric field, including charge trapping in the bulk of the semiconducting material [23], surface polarization,[24] depletion region due to Schottky contacts [25] or ion accumulation at the vicinity of the contact electrodes.[26] All of these potential mechanisms may lead to mis-estimation of the values of $\mu\tau$ products in $MAPbBr_3$-based detectors using Eq. 2. To date, the hypothesis of ion accumulation seems to be the prevailing one in the literature on perovskite detectors.[26], [27] Considering the numerous works on the migration of ionic species in $MAPbBr_3$,[28]–[31] it seems to be the most possible explanation to the best of our knowledge.

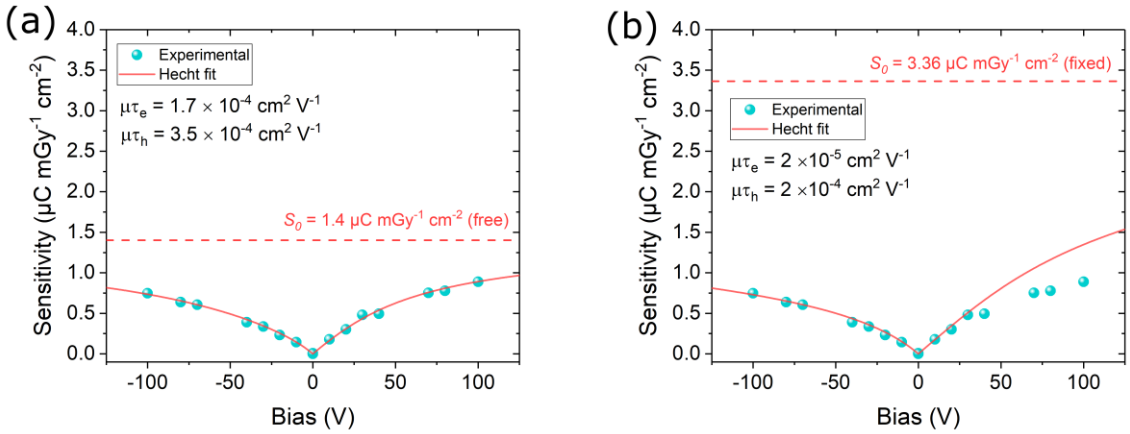

Fig. 1. Sensitivity-voltage plots of a $MAPbBr_3$ device with corresponding two-carriers Hecht fits with (a) S_0 set as a free parameter and (b) S_0 set as the total charge generated in the device. See Methods for more details on the calculation of S_0.

Another intriguing feature of our $MAPbBr_3$-based devices arises from the so-called *bias memory effect* in short-circuit conditions. As notified in previous works, after biasing, $MAPbBr_3$ and other halide perovskites devices exhibit transient dark current relaxation with inverted sign at 0V.[19], [32] In addition the dark current transient is accompanied with non-negligible sensitivity under X-rays during the relaxation window at 0V, as shown in Fig.2(c). Notably, the sensitivity at 0V decays over time with slow dynamics akin to the dark current transient (Fig.S5). Fig.2(d-e-f) provides a depiction of the *bias memory effect*. Several works suggest that upon biasing, the displacement of mobile ions toward the contact electrodes builds up a space-charge that distorts the electric field (Fig.2d and 2e).[27], [33] Consequently the net electric field in the bulk region of the device is reduced with respect to the uniform case (dotted blue line in Fig. 2e). [19][27] In the present work, we approximate the electric field in the bulk to $\frac{V-Vi}{L-wi}$ where Vi is the potential drop associated to the space-charge formation, wi the total space-charge width. When the bias is subsequently released, the space-charge built-up by the accumulations of ions prevails and creates a residual electric field that we approximate to $\frac{Vi}{L-wi}$ in the bulk region (Fig. 2f). Note that during both biasing and recovery steps, we deem the electric field to be flat in the bulk region of the detector and non-uniform in the space-charge regions, in accordance with previous works.[19], [26] After bias removal, the residual field during the recovery step gradually fades out as the mobile ions return to equilibrium. It should be noted again that the present work does not assume an origin for the internal electric field, which can originate from any space charge build-up in the perovskite material. Nonetheless, the migration of mobile ions provides a comprehensive picture to describe these results, as depicted in the schematics of Fig.2d. In this picture, the dark current recovery measured at 0V would originate from an interplay between ionic and electronic currents[19]; and the photogenerated charge carriers may drift along the residual electric field at 0V during a characteristic recovery time, thus generating decaying photocurrent over time (Fig. 2c).

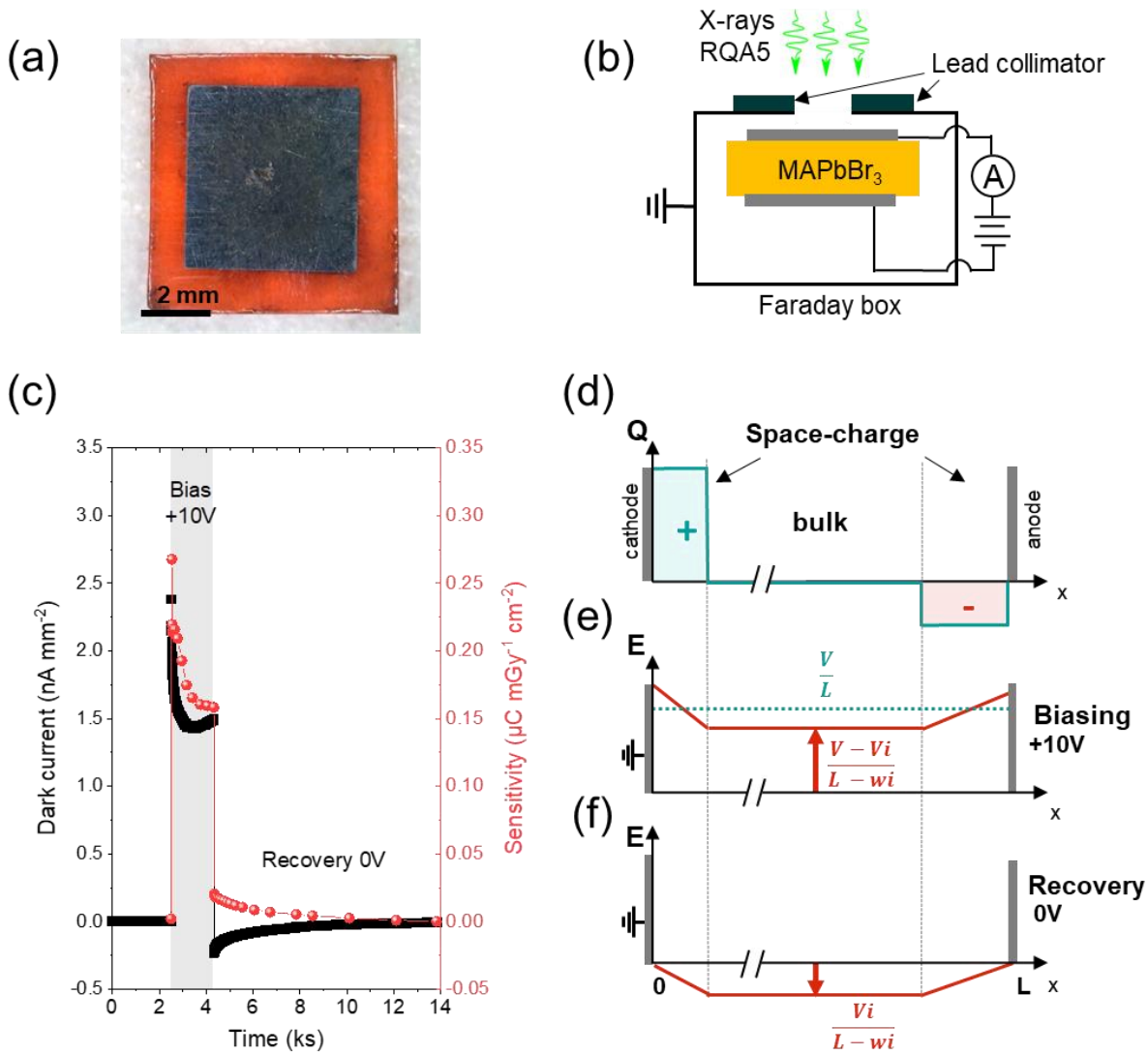

Fig. 2. (a) Microscope picture of a typical Cr/$MAPbBr_3$/Cr single crystal device used in this study. (b) Schematic of the X-ray irradiation setup. (c) Dark current (black curve) and sensitivity-time (red curve) measurements during both biasing et recovery steps. (d-e-f) Proposed model for the electric field profile in the depth of the device during the experiment. The electric field is supposed linear in the bulk and is approximated by $\frac{V-Vi}{L-wi}$ during the biasing step (e), and $\frac{Vi}{L-wi}$ during the recovery step (f).

Fig.3 gives additional insights about the residual electric field for a Cr/$MAPbBr_3$/Cr single crystal device. For the moderate biasing time range (400-2000 seconds) and applied bias (10V) used in this experiment, the sensitivity at 10V decreases slightly over time (Fig.3a). We attribute this to the space-charge build-up that gradually reduces the net electric field in the bulk region of the device, with a consequent reduction of the sensitivity.[27] When the bias is released, sensitivity is measured at 0V owing to the residual electric field. Notably, the sensitivity measured at 0V immediately after removing the bias is the same regardless of the biasing duration in the [400-1800s] bias duration range investigated in this work (Fig.3a). It suggests that, for this 2-mm thick $MAPbBr_3$ device, the space-charge build-up is rather fast (≤400 seconds) and remains constant. Thus, the sensitivity of the device at 0V is initially the same for biasing duration ≥400s. In addition, the residual electric field varies with the applied bias. As seen in Fig 3b, the sensitivity at 0V measured immediately after removing the bias scales with the previous bias value accordingly, indicating that the space-charge build-up is a function of the applied electric field; that could indicate the drifting of mobile ionic species.[30], [31] However,

we noted only a 30% increase in the residual sensitivity at 0V with bias increasing from 10V to 150V, which would suggest that most of the mobile ions have already reach the electrode for biases ≥10V and biasing duration ≥400 seconds. Markedly, this experiment could partially explain why the experimental *S-V* is not well fitted with the Hecht equation in Fig.1b. Along with the rising space-charge that produces distortion of the electric field at high bias, the net electric field in the bulk is progressively reduced by the internal field build-up as the applied bias is increased. As a consequence, the net electric field in the device can be underestimated, as it will be discussed below. Finally, the dynamics of the transient sensitivity at 0V may provide further information on the mobility and the concentration of mobile ionic species in the material. This will be discussed in a future work. In the present work, we will focus on the sensitivity at 0V measured immediately after removing the bias, and develop a model that accords accurately the above-mentioned results.

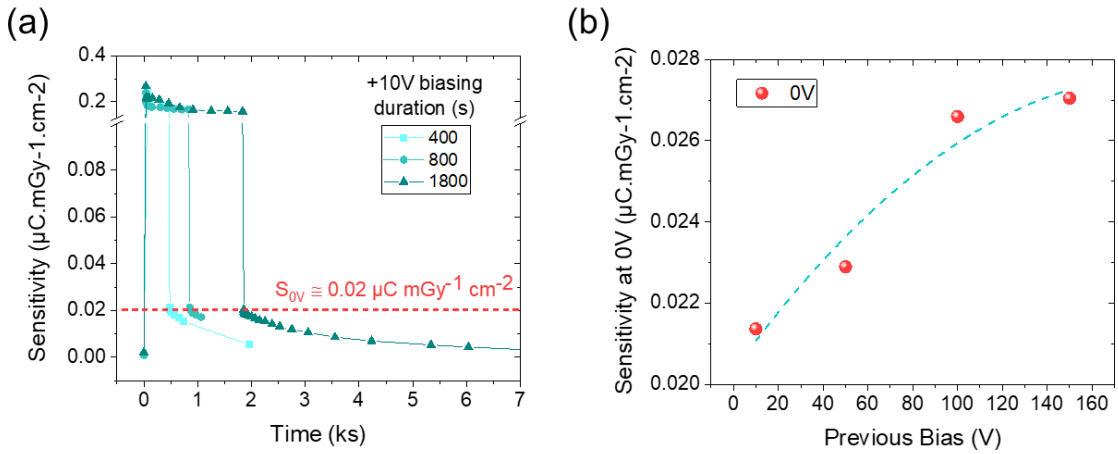

Fig. 3. (a) Sensitivity-time measurements for different biasing duration at +10V (b) Sensitivity measured immediately after removing the bias for different previously applied bias. The biasing duration is 400 seconds. Blue dotted line is an eye guideline.

4. Model

In the following, we propose to model the sensitivity of a 2-mm thick $MAPbBr_3$ planar device considering the following assumptions : (i) the electric field is mainly uniform throughout the device; (ii) an internal electric field is created upon biasing, and is equivalent to the residual electric field at 0V immediately after removing the bias ; (iii) the internal electric field opposes the externally applied electric field (see Fig.3a). Regarding (i), the simulations carried out by Alvarez *et al.* show that the accumulation of mobile ions forms a depletion region at the very vicinity of the electrodes, with a depletion width only up to a few micrometers when the device is previously biased at 10V.[19] Besides, the electric field as function of the depth is mostly flat in the bulk,[19], [26] and for a 2-mm thick device wi<<L, thus the internal field in the bulk region is approximated by $\frac{Vi}{L}$ (Fig. 4). We can consider a uniform electric field in the sensitivity model provided that the penetration depth of the X-rays is much greater than the depletion width. In the present case, the hard RQA5 X-rays with a high mean energy of 53 keV generate charges throughout the volume of the 2-mm thick $MAPbBr_3$ device, as evidenced in Fig.4c (dotted line). In addition, we limit our model to rather moderate applied bias (10V), for which the electric field distortion is limited. Finally, the assumptions (ii) and (iii) are justified by the dark current and sensitivity-time measurements displayed in Fig.2 and Fig.3.

Due to high penetration depth of the X-rays used in the present study, using the two-carriers Hecht equation (3) is compulsory. Considering the assumptions listed above, the model reads as follow. The sensitivity under bias measured a fraction of time before removing the bias writes:

$$S(V-Vi) = \int s_0(x)\eta_{bias}(x, V-Vi)dx \tag{5}$$

$$\eta_{bias}(x, V-Vi) = \frac{\mu_e\tau_e(V-Vi)}{L^2}\left[1-e^{-\frac{L(L-x)}{\mu_e\tau_e(V-Vi)}}\right] + \frac{\mu_h\tau_h V}{L^2}\left[1-e^{-\frac{xL}{\mu_h\tau_h(V-Vi)}}\right] \tag{6}$$

The sensitivity at 0V measured immediately after removing the bias writes :

$$S(Vi) = \int s_0(x)\eta_{short}(x, Vi)dx \tag{7}$$

$$\eta_{short}(x, Vi) = \frac{\mu_e\tau_e Vi}{L^2}\left[1-e^{-\frac{xL}{\mu_e\tau_e V}}\right] + \frac{\mu_h\tau_h Vi}{L^2}\left[1-e^{-\frac{L(L-x)}{\mu_h\tau_h Vi}}\right] \tag{8}$$

Where V is the externally applied bias, Vi is the potential associated to the internal electric field $= \frac{Vi}{L}$, η_{bias} is the CIE before removing the bias and η_{short} is the CIE after removing the bias and x is the position of interaction of the X-ray in the $MAPbBr_3$ device. Note that the equations (6) and (8) correspond to the case where a positive bias is applied to the irradiated electrode. For a 2-mm thick $MAPbBr_3$ device and borderline hard ~50 keV X-rays, the response in biasing conditions is slightly dominated by hole transport (Fig.4a), and the response in short-circuit conditions is slightly dominated by electron transport (Fig.4b). Fig. 4c displays the results of the model calculation for the following input parameters : $\mu_e\tau_e$ = 1.10^{-4} cm^2 V^{-1} ; $\mu_h\tau_h$ = 2.10^{-4} cm^2 V^{-1} ; L = 0.2 cm ; V = 10V ; Vi = 1V. It can be seen that the total induced charge under X-rays – or in other word, the sensitivity S – is close to the experimental value shown in Fig.3a (S ≈ 0.2 µC mGy^{-1} cm^{-2} at 10V and S ≈ 0.02 µC mGy^{-1} cm^{-2} at 0V). Notably, it implies that the internal electrical field at 10V could be as high as 5 V/cm ; which corresponds to 10 percent of the externally applied electric field (50 V/cm). It indicates that there could be a 10% uncertainty on the value of the applied bias that could partially explain the discrepancy between the *S-V* plot and the Hecht model, as depicted in Fig.1b.

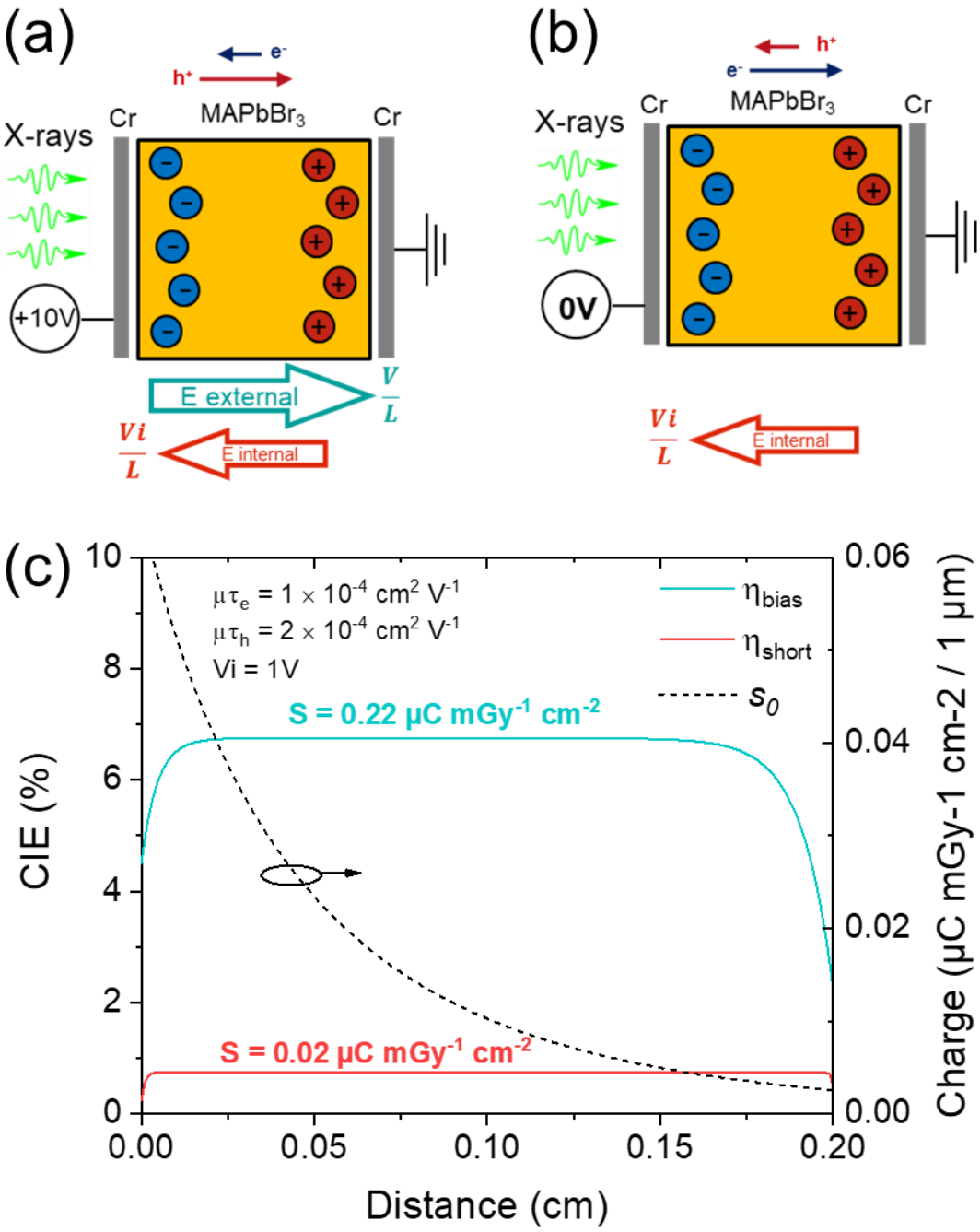

Fig. 4. Schematics of the device during (a) the biasing condition and (b) the short-circuit condition. The internal and external electric fields are deemed uniform throughout the device (c) Results of the calculation. Blue and red lines are the CIE as function of distance at 10V and 0V respectively. Black dotted line is the photogenerated charge. The x-axis is the distance in the device from the irradiated electrode (x=0) to the back electrode (x=L=2mm). Calculated for RQA5 X-rays.

5. Results and discussion

In this part, it will be demonstrated how the model allows to estimate precisely the internal electric field in a Cr/$MAPbBr_3$/Cr planar device, as well as reasonable ranges for the $\mu_e\tau_e$ and $\mu_h\tau_h$ products.

The set of equation (5-8) has 3 unknown parameters : $\mu_e\tau_e$; $\mu_h\tau_h$ and Vi. Only two experimental measurement of sensitivity are used as inputs for the model : S at 10V before removing the bias, and S at 0V immediately after removing the bias. Hence it may provide only a set of solution ($\mu_e\tau_e$, $\mu_h\tau_h$,Vi). Nonetheless, we will see that the set of possible solution is limited and allow to establish a credible range for the above cited parameters.

The model was applied to the measurements displayed in Fig.3a for a $MAPbBr_3$ single crystal planar device with 2-mm thickness, 5 x 5 mm² chromium electrodes and RQA5 X-rays. The picture of the device is shown in Fig. 2a. Further details on the fabrication of the device and the experimental setup are supplied in the Methods section. The experimental measurement of sensitivity gives : S(10-Vi) = 0.17 µC mGy^{-1} cm^{-2} and S(Vi) = 0.021 µC mGy^{-1} cm^{-2}. We calculated all the possible ($\mu_e\tau_e$, $\mu_h\tau_h$,Vi) for which S(10-Vi) and S(Vi) are both equal to the above cited values at the same time. The Fig.5a. displays the results of the calculation in the ($\mu_e\tau_e$, $\mu_h\tau_h$) space. For all Vi, S(10-Vi) and S(Vi) form two straight lines that only cross for a limited number of Vi values ranging from 0.9 V to 1.2 V. The intersection of the two S(10-Vi) and S(Vi) lines implies that it exists a set of ($\mu_e\tau_e$, $\mu_h\tau_h$,Vi) that allows to fully describe the experimental sensitivity measured under X-ray, or in other word, it provides a solution of the equation system. Hence, all the possible solutions (intersections) for this experiment are displayed in Fig. 5b. It allows us to establish that the internal electric field $Ei = \frac{Vi}{L}$ is in the range [4.4 – 5.6] V/cm, or is equal to 5.1 V/cm with 15% uncertainty. Regarding the possible values for ($\mu_e\tau_e$, $\mu_h\tau_h$), the range of solutions is much broader. $\mu_e\tau_e$ spans from 5 x 10^{-6} cm^2 V^{-1} to 3 x 10^{-4} cm^2 V^{-1} and $\mu_h\tau_h$ spans from 1 x 10^{-7} cm^2 V^{-1} to 2.5 x 10^{-4} cm^2 V^{-1}. The uncertainty on the individual $\mu_e\tau_e$ and $\mu_h\tau_h$ values is therefore very high with this model. Nonetheless, more notable is the fact that this experiment computes quite precisely a value for the sum $\mu_e\tau_e + \mu_h\tau_h$, as displayed by the linear fit in Fig. 5b. All of these solutions are aligned, and the sum $\mu_e\tau_e + \mu_h\tau_h$ has a near constant value of ~2.5 x 10^{-4} cm^2 V^{-1}. Here, the range of solutions is a straight line because we are dealing with small electric fields, which means that the mean free path of the charge carriers is small compared to the thickness of the device. In that peculiar case, the exponential term in the Hecht equation becomes negligible, and the CIE becomes $\simeq \frac{\mu_e\tau_e V}{L^2} + \frac{\mu_h\tau_h V}{L^2} = \frac{(\mu_e\tau_e+\mu_h\tau_h)V}{L^2}$. Substituting this into equation 7 gives 2.6 x 10^{-4} cm^2 V^{-1} for Vi =1V, which is consistent with the above results. The information on the sum $\mu_e\tau_e + \mu_h\tau_h$ provides new insights into the charge transport properties of the material. Using other complementary measurements, it is then possible to fully rationalize the transport of the material. For instance, the rather symmetric S-V plot displayed in Fig.1. indicate that the respective $\mu_e\tau_e$ and $\mu_h\tau_h$ values probably have the same order of magnitude. Otherwise, the S-V data would be very asymmetrical for the X-ray exposure conditions and device thickness used in this work. (see supplementary Fig.S6). This is consistent with photocurrent measurements made under the AM-241 source, which indicate that the $\mu_e\tau_e$ and $\mu_h\tau_h$ could be separated only by a factor of 2.[34], [35]

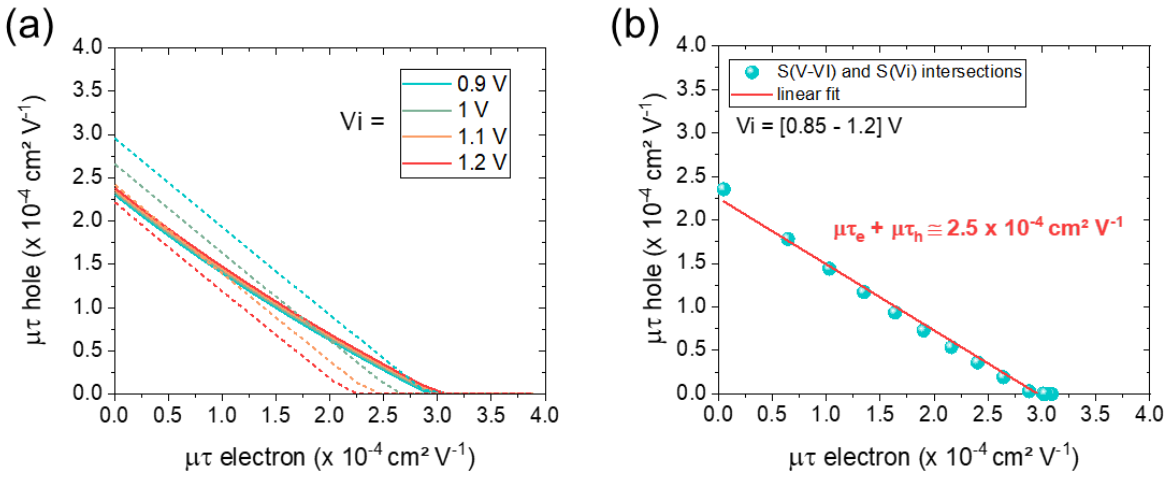

Fig.5. Calculations of the ($\mu_e\tau_e$, $\mu_h\tau_h$,Vi) solutions for S(10-Vi) = 0.17 µC mGy^{-1} cm^{-2} (solid lines) and S(Vi) = 0.021 µC mGy^{-1} cm^{-2} (dash lines). (a) S(10-V) and S(Vi) lines as function of Vi. Each color corresponds to a different Vi input value. (b) Intersections of the S(10-V) and S(Vi) lines with Vi varying from 0.85 to 1.2V.

To assess the robustness of the method, we simulated the response of $MAPbBr_3$ devices for hypothetical ($\mu_e\tau_e$, $\mu_h\tau_h$,Vi) and thickness values. Several of these simulations are displayed in Fig.6. Remarkably, we noticed that it does not seem to exist a case where the two S(10-Vi) and S(Vi) lines doesn't cross in one point in the ($\mu_e\tau_e$, $\mu_h\tau_h$) space for a single Vi value. As seen in Fig. 6a and 6b, the lines are almost parallel when the ($\mu_e\tau_e$, $\mu_h\tau_h$) values are moderate (≤ 1 x 10^{-4} cm^2 V^{-1}). When the charge transport is better (≈ 1 x 10^{-3} cm^2 V^{-1}) as in Fig 6c, the model still provides a single solution for a single Vi value. In the latter case however, the S(V-Vi) line is no longer parallel to the S(Vi) line. It implies that the error on Vi is much higher than in the moderate charge transport case since the position of the S(Vi) line varies sizably with the Vi value (Fig. 6a-b). It can be understood by considering that high sensitivity increases the total number of possible solutions for the model. If the transport is high, the sensitivity is high accordingly, and the model struggles to resolve accurately a value for Vi. If such a case were to be met, a quick fix would consist of reducing the applied bias V in order to reduce the charge carrier mean free path. As seen in Fig. 6d, it results in a reduction of the curvature of the S(V-Vi), and an increased precision on the estimation of Vi. In addition, having straight S(V-Vi) and S(Vi) lines is associated to a low mean free path for the charge carriers, which allows to establish accurately a value of the sum $\mu_e\tau_e + \mu_h\tau_h$ (see Fig. 5b). Lowering the bias during the biasing step to reduce the mean free path is thus interesting to increase the precision for both the internal potential Vi, and the sum of the mobility lifetime products $\mu_e\tau_e + \mu_h\tau_h$.

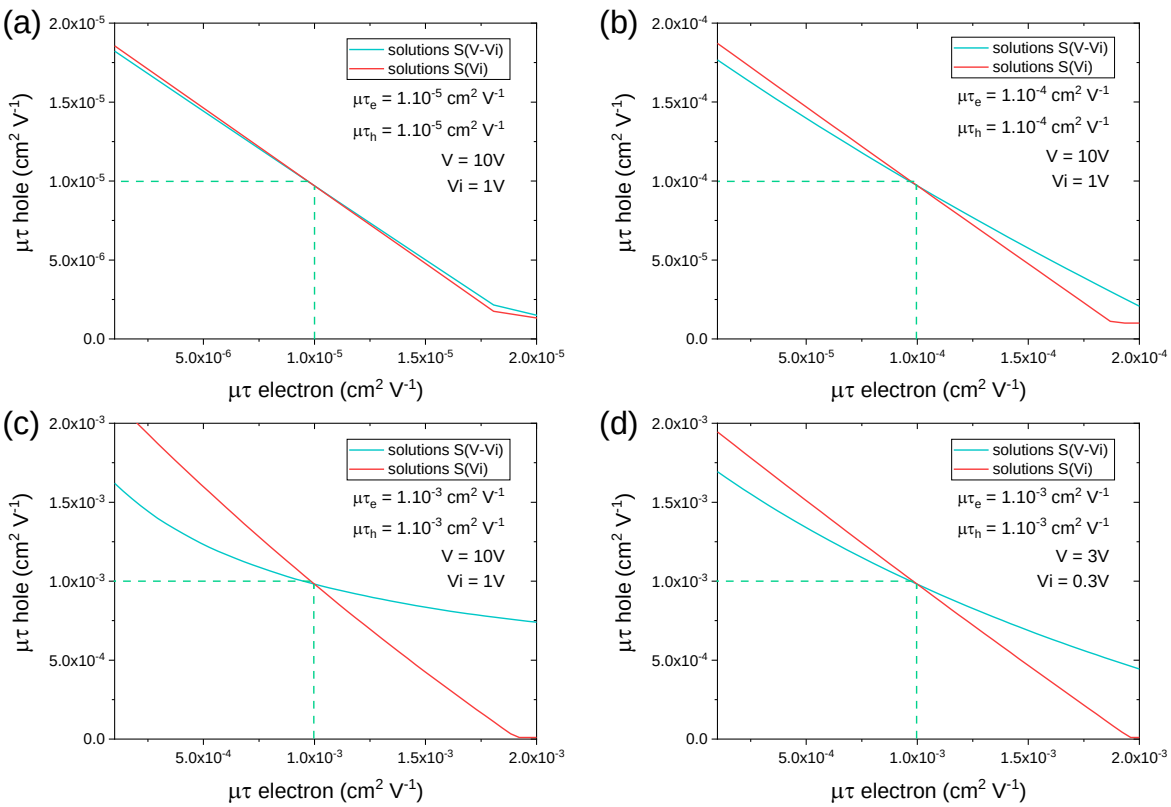

Fig. 6. Calculation of the S(V-Vi) and S(Vi) lines for different ($\mu_e\tau_e$, $\mu_h\tau_h$,Vi) input values. The thickness of the device is 2 mm. The intersection of the S(V-Vi) and S(Vi) lines provides the solution of the equation system.

Finally, we can use this model to estimate an order of magnitude for the space-charge density generated upon biasing. First, we considered the parallel plate capacitor approximation which reads $\mathrm{Q} = \mathrm{C} \times \mathrm{V}$ and $Q = \frac{\varepsilon\varepsilon_0 S}{L}$ with Q the charge, C the capacity, ε the relative permittivity of the perovskite, ε_0 the vacuum permittivity, S the electrode surface area and L the device thickness. From the Fig.5, we can assume a value for Vi ≈ 1V, corresponding to a charge of 50 nC. If we assume that this charge was extracted from the bulk of the crystals, e.g. via migration of charged ionic species, and that the totality of the charges reached the electrode, we can establish that the charge density in the bulk was initially 1 µC cm^{-3}. Now if we consider that this charge originate from moving ionic species, it would represent a density of 10^{+13} ions cm^{-3}, which is in accordance with ionic concentrations previously measured in similar $MAPbBr_3$ single crystal devices.[19], [36]

6. Conclusion

In this paper, we provide robust experimental evidences for the presence of an internal electric field in Cr/$MAPbBr_3$/Cr X-ray detectors that builds up upon biasing. This internal electric field generates a significant but decaying response under X-rays at 0V; and diminish the net electric field in the device under bias. We propose that the discordance between the experimental *S-V* plots and the Hecht model is due to the internal electric field that alters the *S-V* relationship. Starting from a modified version of the Hecht equation, we developed a model for the sensitivity that involves an internal electric field with opposed sign to the externally applied electric field. We found that the model can accurately

predict a value for the internal electric field, even without prior information about the charge transport properties of the material. Notably, the actual internal electric field in the bulk of our 2-mm $MAPbBr_3$ device could be overestimated by about 10% at 50V/cm. In addition, we exploit our model as an alternative pathway for the evaluation of the $\mu_e\tau_e$ and $\mu_h\tau_h$ products, and more precisely for the sum $\mu_e\tau_e + \mu_h\tau_h$. We believe that our model rationalize some intriguing electrical properties of $MAPbBr_3$ detectors under bias such as dark current relaxation and zero-bias sensitivity; and could be extended to other perovskite composition exhibiting dark current relaxation at zero-bias such as $CH_3NH_3PbI_3$ and $CsPbBr_3$.[32], [37] Future work will bring further information on the remnant charge density in the $MAPbBr_3$ material by exploiting the dynamics of sensitivity decay at zero-bias.

Methods

Device Fabrication

Millimeter-sized methylammonium lead tribromide ($MAPbBr_3$) single crystals were grown using the Modified Inverse Temperature Crystallization (MITC) method described in details in previous works.[9], [16], [19] Briefly, the precursor solutions were prepared in an argon-filled glovebox by dissolving $PbBr_2$ (ultra dry, 99.999 % metal basis) and MABr (≥99 %) in anhydrous N,N-Dimethylformamide with 1:1 molar ratio. The growth was carried out using a crystal seed, as described in [9]. Both the large facets of the crystals were mechanically polished with SiC disks and isopropanol, then with fabric disks and diamond paste in order to obtain a mirror grade quality. 100-nm Cr electrodes were subsequently thermally evaporated on both facets. We found that proper polishing and chromium electrodes enhance the electrical stability of the devices under bias, as also noted in previous works.[15], [38]

X-ray characterization

Dark current and sensitivity measurements were conducted on the same setup using a Keithley 428 current amplifier and a Keithley 487 power supply. The samples were irradiated with short X-ray pulses (4 Hz repetition rate, 100 ms duration) using a medical-grade pulsed X-ray tube with tungsten anode and 70 kVp accelerating voltage. The incident X-rays were filtrated through a 0.8 mm beryllium window and 23.5 mm additionnal aluminium filters to yield a RQA5 spectrum, following the IEC 62220 International Standard. The incident dose was calibrated with a PTW Unidos dosimeter, yielding 24 ± 0.6 μGy_{air} per pulse. The X-rays were collimated through a 12.6 mm² hole pierced in a ≈5mm-thick lead plate. Due to long-range diffusion of the X-ray generated charge carriers in the area not covered by the electrodes, the collimation is necessary to properly evaluate the absorption surface area of the incident X-rays, hence the sensitivity. Each sensitivity measurement consisted of 10 X-ray pulses that were averaged to reduce experimental error (see Fig. S7). Typical uncertainty on the sensitivity measurement was 3%.

Numerical simulation

The elemental charge deposited in the $MAPbBr_3$ material s_0 and the maximum theoretical sensitivity S_0 were calculated using Eq. 9 and Eq. 10 that read:

$$S_0(x) = \frac{e \times E^*(x)}{W_\pm} \tag{9}$$

$$E^*(x) = \int N(E) \times E \times A(x,E)\, dE \tag{10}$$

Where e is the elemental charge ; E^* is the energy deposited by the X-rays in the perovskite material (Fig. S8), $W_{\pm}$ is the electron-hole pair creation energy that was calculated using Klein's rule $W_{\pm} = \frac{14}{5}E_g + 0.5$ with E_g = 2.3 eV [16], [21] ; D is the dose per surface area ; N is the number of incident photon emitted by the X-ray tube as function of photon energy E; A is the absorbed fraction as function of the position of interaction of the X-rays in the MAPbBr3 device. The latter is computed as for Eq. 11 :

$$A(x,E) = T(x,E) - T(x+dx,E) = e^{-\sigma(E)\rho x} - e^{-\sigma(E)\rho(x+dx)} \tag{11}$$

Where T is the transmitted fraction; σ is the photon cross section; ρ is the density (3.8 g cm^{-3} for $MAPbBr_3$)[39]. The photon cross section was obtained from NIST photon cross sections database considering only the photoelectric interaction, assuming that it is the predominant interaction mechanism in the 20-70 keV energy range for $MAPbBr_3$.[40] The number of incident photon$s$ N was computed for a RQA5 spectrum using the SpekCalc software.[41]–[43] It is given as function of incident X-ray dose in mGy_{air} and per unit area (Fig. S9).

Supplementary Material

The Supplementary Material is available free of charge at:

Additionnal Hecht equation fitting plots, computations of the energy deposited by the X-rays and the number of incident photons, examples of X-ray-induced photocurrent pulses under bias and at short-circuit.

Author Declaration section

Conflict of Interest Statement

The authors have no conflicts to disclose.

Author Contributions

F.L.: conceptualization, X-ray characterizations, computations, writing-original draft ; J.M-G. and S.L.: crystal growth, device fabrication ; J.Z. and J-M.V.: investigations, writing-review and editing , project administration ; E.G.-D.: conceptualization, methodology, writing−review and editing.

Data Availability Statement

The data that support the findings of this study are available from the corresponding authors upon reasonable request.

Acknowledgement

This work has received funding from the European Union's Horizon 2020 research and innovation program under the Photonics Public−Private Partnership (www.photonics21.org) with the project PEROXIS under grant agreement N° 871336.

References

[1] H. Wei *et al.*, « Sensitive X-ray detectors made of methylammonium lead tribromide perovskite single crystals », *Nature Photon*, vol. 10, nº 5, p. 333-339, mai 2016, doi: 10.1038/nphoton.2016.41.

[2] W. Wei *et al.*, « Monolithic integration of hybrid perovskite single crystals with heterogenous substrate for highly sensitive X-ray imaging », *Nature Photon*, vol. 11, nº 5, p. 315-321, mai 2017, doi: 10.1038/nphoton.2017.43.

[3] X. Wang *et al.*, « PIN Diodes Array Made of Perovskite Single Crystal for X-Ray Imaging », *physica status solidi (RRL) – Rapid Research Letters*, vol. 12, nº 10, p. 1800380, oct. 2018, doi: 10.1002/pssr.201800380.

[4] Q. Xu *et al.*, « High-Performance Surface Barrier X-ray Detector Based on Methylammonium Lead Tribromide Single Crystals », *ACS Appl. Mater. Interfaces*, vol. 11, nº 10, p. 9679-9684, mars 2019, doi: 10.1021/acsami.8b21605.

[5] L. Li *et al.*, « Enhanced X-ray Sensitivity of MAPbBr3 Detector by Tailoring the Interface-States Density », *ACS Appl. Mater. Interfaces*, vol. 11, nº 7, p. 7522-7528, févr. 2019, doi: 10.1021/acsami.8b18598.

[6] X. Geng *et al.*, « High-Quality Single Crystal Perovskite for Highly Sensitive X-Ray Detector », *IEEE Electron Device Lett.*, vol. 41, nº 2, p. 256-259, févr. 2020, doi: 10.1109/LED.2019.2960384.

[7] W. Zhang, H. Wang, H. Dong, F. Li, Z. Wang, et Y. Shao, « Mechanical polishing with chemical passivation of perovskite single crystals for high-performance X-ray detectors », *J. Mater. Chem. C*, vol. 10, nº 45, p. 17353-17363, 2022, doi: 10.1039/D2TC03850A.

[8] M. I. Saidaminov *et al.*, « High-quality bulk hybrid perovskite single crystals within minutes by inverse temperature crystallization », *Nat Commun*, vol. 6, nº 1, p. 7586, nov. 2015, doi: 10.1038/ncomms8586.

[9] S. Amari, J.-M. Verilhac, E. Gros D'Aillon, A. Ibanez, et J. Zaccaro, « Optimization of the Growth Conditions for High Quality $CH_3NH_3PbBr_3$ Hybrid Perovskite Single Crystals », *Crystal Growth & Design*, vol. 20, nº 3, p. 1665-1672, mars 2020, doi: 10.1021/acs.cgd.9b01429.

[10] F. Yao *et al.*, « Room-temperature liquid diffused separation induced crystallization for high-quality perovskite single crystals », *Nat Commun*, vol. 11, nº 1, p. 1194, mars 2020, doi: 10.1038/s41467-020-15037-x.

[11] K. Hecht, « Zum Mechanismus des lichtelektrischen Primärstromes in isolierenden Kristallen », *Z. Physik*, vol. 77, nº 3-4, p. 235-245, mars 1932, doi: 10.1007/BF01338917.

[12] T. E. Schlesinger et R. B. James, *Semiconductors for Room Temperature Nuclear Detector Applications*, Academic Press., vol. 43. in Semiconductors and Semimetals, vol. 43. 1995.

[13] G. Bertolini et A. Coche, *Semiconductor Detectors*, Eds. Interscience. Wiley, 1968.

[14] J. Song *et al.*, « Facile Strategy for Facet Competition Management to Improve the Performance of Perovskite Single-Crystal X-ray Detectors », *J. Phys. Chem. Lett.*, vol. 11, nº 9, p. 3529-3535, mai 2020, doi: 10.1021/acs.jpclett.0c00770.

[15] R. Tan *et al.*, « Characterization of solution grown 3D polycrystalline methylammonium lead tribromide for x-ray detection », *Journal of Applied Physics*, vol. 132, nº 20, p. 204503, nov. 2022, doi: 10.1063/5.0100362.

[16] J. M. Guillén *et al.*, « MAPb(Br1–xClx)3 Hybrid Perovskite Materials for Direct X-ray Detection », mars 2023, doi: https://doi.org/10.1021/acsaelm.3c00114.

[17] Z. Gou *et al.*, « Self-Powered X-Ray Detector Based on All-Inorganic Perovskite Thick Film with High Sensitivity Under Low Dose Rate », *Phys. Status Solidi RRL*, vol. 13, nº 8, p. 1900094, août 2019, doi: 10.1002/pssr.201900094.

[18] K. Sakhatskyi *et al.*, « Stable perovskite single-crystal X-ray imaging detectors with single-photon sensitivity », *Nat. Photon.*, mai 2023, doi: 10.1038/s41566-023-01207-y.

[19] A. O. Alvarez *et al.*, « Ionic Field Screening in MAPbBr3 Crystals Revealed from Remnant Sensitivity in X-ray Detection », *ACS Phys. Chem Au*, p. acsphyschemau.3c00002, mai 2023, doi: 10.1021/acsphyschemau.3c00002.
[20] S. Ramo, « Currents Induced by Electron Motion », *Proc. IRE*, vol. 27, nº 9, p. 584-585, sept. 1939, doi: 10.1109/JRPROC.1939.228757.
[21] C. A. Klein, « Bandgap Dependence and Related Features of Radiation Ionization Energies in Semiconductors », *Journal of Applied Physics*, vol. 39, nº 4, p. 2029-2038, mars 1968, doi: 10.1063/1.1656484.
[22] Y. He *et al.*, « High spectral resolution of gamma-rays at room temperature by perovskite CsPbBr3 single crystals », *Nat Commun*, vol. 9, nº 1, p. 1609, déc. 2018, doi: 10.1038/s41467-018-04073-3.
[23] M. Zanichelli, A. Santi, M. Pavesi, et A. Zappettini, « Charge collection in semi-insulator radiation detectors in the presence of a linear decreasing electric field », *J. Phys. D: Appl. Phys.*, vol. 46, nº 36, p. 365103, sept. 2013, doi: 10.1088/0022-3727/46/36/365103.
[24] F. Principato, A. A. Turturici, M. Gallo, et L. Abbene, « Polarization phenomena in Al/p-CdTe/Pt X-ray detectors », *Nuclear Instruments and Methods in Physics Research Section A: Accelerators, Spectrometers, Detectors and Associated Equipment*, vol. 730, p. 141-145, déc. 2013, doi: 10.1016/j.nima.2013.05.157.
[25] H. Meng *et al.*, « Simulation of the Charge Collection in a Nonuniform Electric Field for MAPbI3 Semiconductor Nuclear Detector With Schottky Contact », *IEEE Trans. Nucl. Sci.*, vol. 69, nº 9, p. 1990-1998, sept. 2022, doi: 10.1109/TNS.2022.3194317.
[26] S. Jia *et al.*, « Ion-Accumulation-Induced Charge Tunneling for High Gain Factor in P–I–N-Structured Perovskite $CH_3NH_3PbI_3$ X-Ray Detector », *Adv. Mater. Technol.*, p. 2100908, déc. 2021, doi: 10.1002/admt.202100908.
[27] O. Baussens *et al.*, « An insight into the charge carriers transport properties and electric field distribution of $CH_3NH_3PbBr_3$ thick single crystals », *Appl. Phys. Lett.*, vol. 117, nº 4, p. 041904, juill. 2020, doi: 10.1063/5.0011713.
[28] Y. Luo *et al.*, « Direct Observation of Halide Migration and its Effect on the Photoluminescence of Methylammonium Lead Bromide Perovskite Single Crystals », *Adv. Mater.*, vol. 29, nº 43, p. 1703451, nov. 2017, doi: 10.1002/adma.201703451.
[29] J. Pospisil *et al.*, « Reversible Formation of Gold Halides in Single-Crystal Hybrid-Perovskite/Au Interface upon Biasing and Effect on Electronic Carrier Injection », *Adv. Funct. Mater.*, vol. 29, nº 32, p. 1900881, août 2019, doi: 10.1002/adfm.201900881.
[30] M. García-Batlle *et al.*, « Moving Ions Vary Electronic Conductivity in Lead Bromide Perovskite Single Crystals through Dynamic Doping », *Adv. Electron. Mater.*, vol. 6, nº 10, p. 2000485, oct. 2020, doi: 10.1002/aelm.202000485.
[31] M. García-Batlle *et al.*, « Coupling between Ion Drift and Kinetics of Electronic Current Transients in MAPbBr3 Single Crystals », *ACS Energy Lett.*, vol. 7, nº 3, p. 946-951, mars 2022, doi: 10.1021/acsenergylett.1c02578.
[32] M. García-Batlle *et al.*, « Mobile Ion-Driven Modulation of Electronic Conductivity Explains Long-Timescale Electrical Response in Lead Iodide Perovskite Thick Pellets », *ACS Appl. Mater. Interfaces*, vol. 13, nº 30, p. 35617-35624, août 2021, doi: 10.1021/acsami.1c06046.
[33] O. Almora, D. Miravel, G. Ilario, et G.-B. Germà, « Long-Term Field Screening by Mobile Ions in Thick Metal Halide Perovskites: Understanding Saturation Currents », *physica status solidi (RRL) – Rapid Research Letters*, nº 16, p. 2200336, 2022, doi: DOI: 10.1002/pssr.202200336.
[34] S. H. Bennett *et al.*, « Charge transport comparison of FA, MA and Cs lead halide perovskite single crystals for radiation detection », *Front. Detect. Sci. Technol.*, vol. 1, p. 1249892, sept. 2023, doi: 10.3389/fdest.2023.1249892.
[35] X. Liu, H. Zhang, B. Zhang, J. Dong, W. Jie, et Y. Xu, « Charge Transport Behavior in Solution-Grown Methylammonium Lead Tribromide Perovskite Single Crystal Using α Particles », *J. Phys. Chem. C*, vol. 122, nº 26, p. 14355-14361, juill. 2018, doi: 10.1021/acs.jpcc.8b03512.
[36] E. A. Duijnstee, V. M. Le Corre, M. B. Johnston, L. J. A. Koster, J. Lim, et H. J. Snaith, « Understanding Dark Current-Voltage Characteristics in Metal-Halide Perovskite Single Crystals », *Phys. Rev. Applied*, vol. 15, nº 1, p. 014006, janv. 2021, doi: 10.1103/PhysRevApplied.15.014006.

[37] B.-B. Zhang *et al.*, « Defect proliferation in CsPbBr3 crystal induced by ion migration », *Appl. Phys. Lett.*, vol. 116, nº 6, p. 063505, févr. 2020, doi: 10.1063/1.5134108.

[38] R. Tan, B. Dryzhakov, J. Charest, B. Hu, M. Ahmadi, et E. Lukosi, « Improved Radiation Sensing with Methylammonium Lead Tribromide Perovskite Semiconductors », *Nuclear Instruments and Methods in Physics Research Section A: Accelerators, Spectrometers, Detectors and Associated Equipment*, vol. 986, p. 164710, janv. 2021, doi: 10.1016/j.nima.2020.164710.

[39] D. Weber, « CH3NH3PbX3, ein Pb(II)-System mit kubischer Perowskitstruktur / CH3NH3PbX3, a Pb(II)-System with Cubic Perovskite Structure », *Zeitschrift für Naturforschung B*, vol. 33, nº 12, p. 1443-1445, déc. 1978, doi: 10.1515/znb-1978-1214.

[40] NIST, « XCOM: Photon Cross Sections Database ». [En ligne]. Disponible sur: https://physics.nist.gov/PhysRefData/Xcom/html/xcom1.html

[41] G. G. Poludniowski et P. M. Evans, « Calculation of x-ray spectra emerging from an x-ray tube. Part I. Electron penetration characteristics in x-ray targets », *Medical Physics*, vol. 34, nº 6Part1, p. 2164-2174, juin 2007, doi: 10.1118/1.2734725.

[42] G. G. Poludniowski, « Calculation of x-ray spectra emerging from an x-ray tube. Part II. X-ray production and filtration in x-ray targets », *Medical Physics*, vol. 34, nº 6Part1, p. 2175-2186, juin 2007, doi: 10.1118/1.2734726.

[43] G. Poludniowski, G. Landry, F. DeBlois, P. M. Evans, et F. Verhaegen, « SpekCalc : a program to calculate photon spectra from tungsten anode x-ray tubes », *Phys. Med. Biol.*, vol. 54, nº 19, p. N433-N438, oct. 2009, doi: 10.1088/0031-9155/54/19/N01.